Difference of rate performance between discharge and charge reactions for bismuth fluoride electrode in lithium-ion battery

Hiroaki Konishi,[a] Taketoshi Minato,[a] Takeshi Abe,[b] and Zempachi Ogumi,[a]

[a]Office of Society-Academia Collaboration for Innovation, Kyoto University, Gokasho, Uji, Kyoto 611-0011, Japan

[b]Graduate School of Engineering, Kyoto University, Nishikyo-ku, Kyoto 615-8510, Japan

Corresponding author

Hiroaki Konishi

E-mail: hiroaki.konishi.yj@hitachi.com

Taketoshi Minato

Mail: minato.taketoshi.5x@kyoto-u.ac.jp

Present address

Hiroaki Konishi

Research & Development Group, Hitachi Ltd.

Hitachi, Ibaraki 319-1292, Japan

E-mail: hiroaki.konishi.yj@hitachi.com

Abstract

The conversion-based BiF_3 is a promising cathode material for lithium-ion batteries due to its high theoretical capacity (302 mAh g^{-1}). Nanocomposites of BiF_3 and carbon (BiF_3/C) are known to improve the electrochemical performance by increasing the electronic conductivity of the electrode. Here we investigate the electrochemical performance of BiF_3/C at high C-rates. In particular, we newly investigate the difference of high C-rate performance between discharge and charge reactions. The discharge and charge capacities in the first cycle were almost the same at 0.1C. In contrast, the discharge capacity was higher than charge capacity at 10C. Further, during cycling at 10C, the charge capacity drastically decreased, but the discharge capacity remained high. The rate performance of the discharge reaction was higher than that of the charge reaction, especially after cycling.

Keywords

1. Introduction

Lithium-ion batteries are utilized in many electronic devices. Recent improvements in device performance have necessitated the development of high-capacity batteries. The main cathode materials in current lithium-ion batteries are intercalation-based materials such as $LiCoO_2$ and $LiMn_2O_4$. However, batteries constructed from such materials have limited capacities [1−3]. Conversion-based cathode materials, which have high theoretical capacities, offer an attractive solution to this problem [4−32]. The conversion reaction progresses according to a following formula (i) [23−25]:

$$MX_m + nLi^+ + ne^- \leftrightarrow M + mLi_{n/m}X \text{ (M: metal and X: anion)} \quad \text{(i)}$$
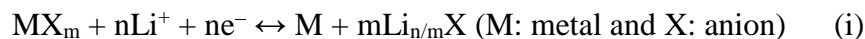
Because the M–F bonds in metal fluorides are more ionic than the M–O bonds in metal oxides, the reaction potential of metal fluorides is higher than that of metal oxides [4, 24, 31]. Therefore, metal fluorides are promising candidates for use as cathode materials. For instance, bismuth fluoride (BiF_3) is a particularly attractive owing to its high theoretical specific capacity (302 mAh g^{-1}); however, the high reactivity of Bi (discharged state) with electrolytes [26, 27] and the low electronic conductivity of BiF_3 (charged state) [23−25] inhibit the charge-discharge reactions in lithium-ion batteries. It has been reported that the surface coating is an effective method to reduce the reaction

between an electrode and electrolyte [28]. The formation of nanocomposites with

carbon (BiF_3/C) can effectively generate an electronic conductive path and improve the

electrochemical properties of BiF_3 [23–25]. Additionally, BiF_3/C exhibits a high

discharge capacity at high C-rates (~200 mAh g^{-1} at ~4C and 24°C) [23]. However, the

effectiveness of BiF_3 as a cathode material for lithium-ion batteries depends on its

electrochemical properties during the charging and cycling of the batteries at high

C-rates, which has not been previously clarified.

In the present study, the electrochemical properties of BiF_3/C at a high C-rate

(10C) during charging and cycling were investigated. Based on the experimental results,

we discuss the difference of high C-rate performance between discharge and charge

reactions.

2. Experimental and theoretical calculation methods

2.1. Preparation of active materials

The BiF_3 powder (Fluorochem Ltd.) was pulverized for 1 h in a planetary ball

mill at 1100 rpm. The resulting material was labeled as BiF_3. Next, 80 wt% of BiF_3 and

20 wt% of acetylene black (AB) were mixed for 1 h in a planetary ball mill at 1100 rpm

to form a nanocomposite composed of BiF_3 and AB. The resulting material was labeled

as BiF_3/C. All samples were placed into a container under an argon atmosphere.

2.2. Electrochemical performance of the prepared samples

The prepared active materials were mixed with AB and polyvinylidene difluoride (PVDF) (BiF_3: AB: PVDF = 60: 25: 15 wt%; BiF_3/C: AB: PVDF = 75: 10: 15 wt%). Then N-methyl-2-pyrrolidone (NMP) solvent was added. The resulting slurry was coated on an Al current collector, and the NMP was removed by heating at 110°C. The loading of electrode was ~2.0 mg cm^{-2}. The discharge/charge capacities of the prepared samples were evaluated using a two-electrode electrochemical cell containing a BiF_3 electrode and lithium metal as the working and counter electrodes, respectively. The electrolyte was a 1.0 M $LiPF_6$ solution in a 3: 7 mixture of ethylene carbonate and diethyl carbonate. The electrochemical cell was assembled in an argon-filled glovebox. The discharge and charge measurements were performed using a potentiostat (Biologic Science Instruments, VMP-300) over the voltage range 2.0–4.5 V at 0.1, 1, and 10C (1C = 302 mA g^{-1}). The measurement temperature was varied as 25 and 55°C.

2.3. Crystal structure of BiF_3/C electrode during the first and the tenth cycles

The crystal structures of the BiF_3/C electrode during the discharge and charge

processes in the first and the tenth cycles were evaluated by X-ray diffraction (XRD).

After the electrochemical cell was discharged and charged, it was decomposed, and the

BiF$_3$/C electrode was washed with dimethyl carbonate. The electrode sealed with a

laminate was used for the XRD measurements. The decomposition of the cell and

sealing of the electrode were carried out in an argon-filled glovebox. The XRD patterns

were recorded with a Rigaku SmartLab diffractometer in the 2θ range 20–50° with Cu

Kα radiation (λ = 1.54 Å).

2.4. Density functional theory calculation to investigate the interaction between Bi and

BiF$_3$

The initial crystal structures of Bi and BiF$_3$ layers were set to trigonal and

hexagonal. The (111) surfaces for Bi and BiF$_3$ were created since these are the stable

surface among Bi and BiF$_3$ surface [33, 34]. The Bi layer was placed above the BiF$_3$

layer. The size of the unit cell is 1.2 nm × 1.2 nm × 6.2 nm. The position of 12 and 36

atoms of Bi and F in the bottom of the BiF$_3$ layer were fixed. The interaction between

Bi and BiF$_3$ was theoretically calculated by density functional theory (DFT) calculations.

The calculations were performed using code CASTEP of Dassault Systemes BIOVIA

[35, 36] with GGA-PBE functional [37] in a condition of spin-polarization considering

the initial spin as the spin state. The interaction was evaluated from the total energy of a

unit cell containing Bi and BiF_3 layers consisted of Bi_{22} and $Bi_{24}F_{72}$ atoms, respectively.

The total energies of the unit cell were calculated varying the position of the Bi layer.

Self-consistent field (SCF) procedures were performed to obtain well-converged

geometrical and electronic structures at a convergence criterion of 5.0×10^{-7} eV atom^{-1}.

The energy, maximum force, and maximum displacement convergence were set to $5.0 \times$

10^{-6} eV atom^{-1}, 1.0×10^{-1} eV nm^{-1}, and 5.0×10^{-5} nm, respectively. Monkhorst-Pack

scheme was used. The calculation was performed with gamma points. The kinetic cutoff

energy used was 440 eV.

3. Results and Discussion

3.1. Electrochemical performance of the prepared samples

Fig. 1 shows the initial discharge-charge curves of BiF_3 and BiF_3/C at 0.1C and

at 25 and 55°C. The discharge/charge capacities of BiF_3 and BiF_3/C at 25°C were

103/21 and 260/267 mAh g^{-1}, respectively. This indicates that the electrochemical

performance of BiF_3 was drastically improved by mixing with AB in the ball mill.

Similar improvements in the discharge/charge capacities of BiF_3 mixed with AB were

reported by Bervas *et al* [23]. Such enhancement might be conferred by the high

adhesion between BiF_3 and the AB particles, which is effective in forming an electronic

conductive path. The discharge/charge capacities were further improved by the increase

in the discharge-charge measurement temperature. The discharge/charge capacities of

BiF_3/C at 55°C (314/319 mAh g^{-1}) were slightly above the theoretical capacity (302

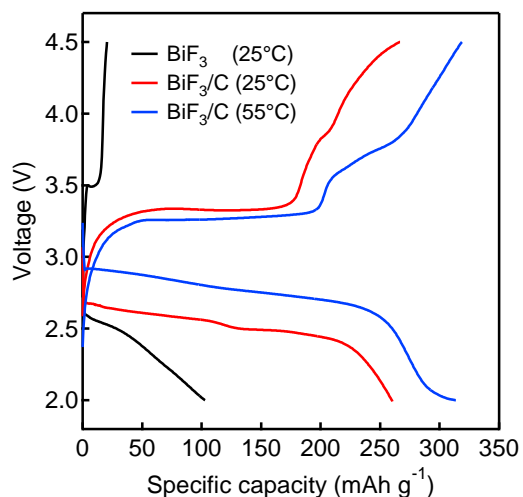mAh g^{-1}). This excess capacity might be attributed to electrolyte decomposition.

Fig. 1. Initial discharge-charge curves of BiF_3 and BiF_3/C at 0.1C and at 25 and 55°C

[BiF_3 at 25°C (black curve), BiF_3/C at 25°C (red curve), and BiF_3/C at 55°C (blue

curve)].

3.2. Crystal structure change during the discharge-charge processes

To confirm the progress of discharge-charge reactions of BiF_3/C at 55°C, the

crystal structure during the discharge-charge processes was evaluated. Fig. 2 shows the

9

XRD patterns of BiF_3/C during the initial discharging and charging. All peaks in the diffraction patterns were assigned to the orthorhombic phase with space group *Pnma* in the pristine state, except for the peak at $2\theta = 28°$, which was indexed to the hexagonal phase with space group *P–3c*1. Increasing the capacity to 100 mAh g^{-1} introduced three new peaks assignable to the trigonal phase with space group *R–3m* (Bi metal), and the fully discharged state (314 mAh g^{-1}) yielded only Bi. In contrast, the new peaks that appeared at a capacity of 206 mAh g^{-1} were attributed to the BiF_3 (hexagonal phase), and the fully charged state (319 mAh g^{-1}) yielded only BiF_3 (hexagonal phase). As previously reported by Bervas *et al.* [23], the crystal structures of BiF_3 differed between the pristine and fully charged states. The XRD findings indicate that the discharge and charge reactions progressed almost to completion with the discharge-charge measurements (blue line in Fig. 1). Collectively, these results demonstrate that BiF_3/C yielded high discharge/charge levels. Therefore, in subsequent experiments, we investigated the high C-rate performance of BiF_3/C at 55°C.
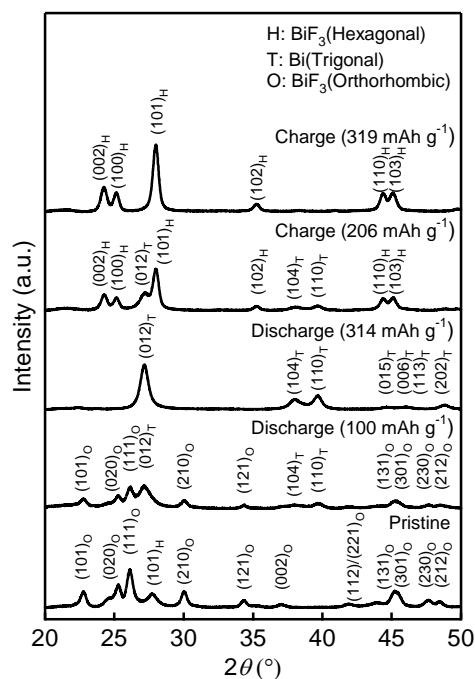
Fig. 2. XRD patterns of BiF$_3$/C during the initial discharge-charge processes [0.1C at 55°C].

3.3. High C-rate performance of BiF$_3$/C at 55°C

Fig. 3 shows the discharge-charge curves of BiF$_3$/C at 55°C over 10 cycles. Here the C-rate was varied as 0.1, 1, and 10C, and the discharge/charge capacities of BiF$_3$/C during the first cycle were measured as 314/319, 261/266, and 197/137 mAh g^{-1}, respectively. Thus, with increasing C-rate, the discharge/charge capacities decreased and the irreversible capacity increased. During the tenth cycle, the discharge/charge capacities of BiF$_3$/C at 0.1, 1, and 10C were 183/194, 187/188, and 31/32 mAh g^{-1}, respectively, revealing a drastic decline in the cycling performance.
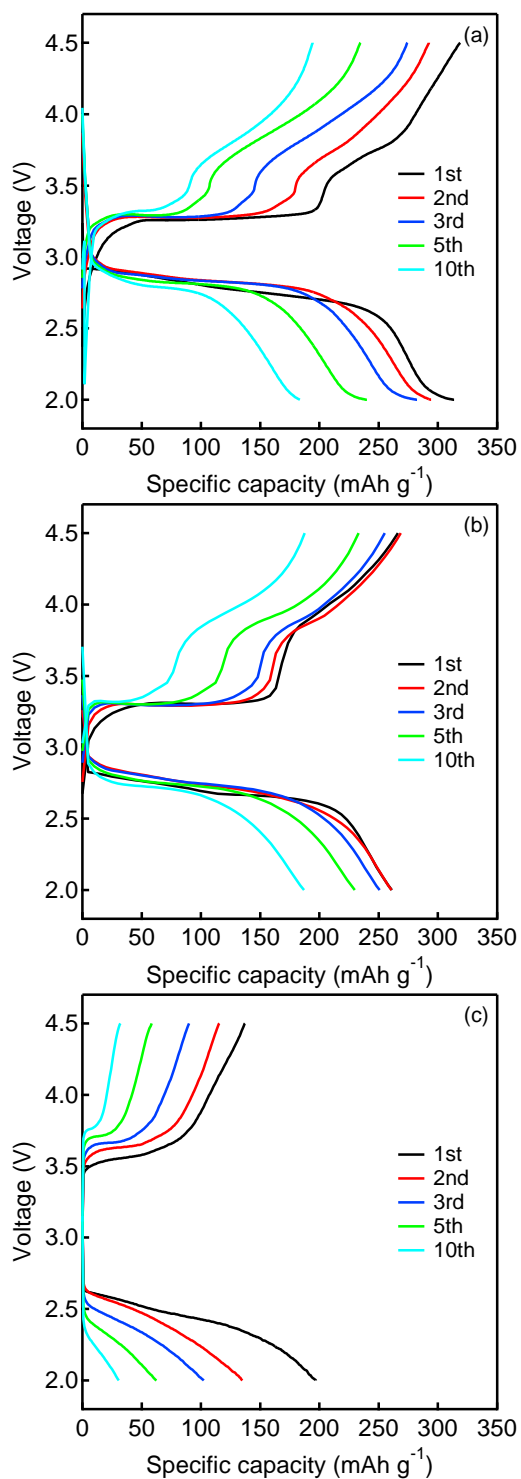
11

Fig. 3. Discharge-charge curves of BiF$_3$/C at 55°C and various C-rates over ten cycles: (a) 0.1C, (b) 1C, and (c) 10C. Black, red, blue, green, and aqua curves represent the discharge-charge curves during the first, second, third, fifth, and tenth cycles, respectively.

To investigate the reaction mechanism in the discharge/charge processes at high C-rates, we analyzed the crystal structures of the active materials by XRD. Fig. 4 shows the XRD patterns recorded during the tenth cycle of BiF_3/C at 10C in the fully discharged (lower pattern) and charged (upper pattern) states. All of the peaks in both states were assigned to Bi metal, except for the peak at $2\theta = 28°$, which was indexed to BiF_3. Therefore, BiF_3/C at 10C mainly comprised Bi metal. The XRD analyses indicate that the charge reaction negligibly proceeded at 10C. The difference in the high C-rate performance between the discharge and charge processes was discussed in Subsections 3.5 and 3.6.
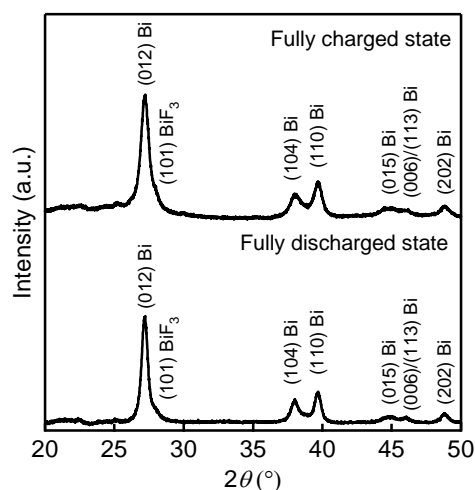

Fig. 4. XRD patterns of BiF_3/C in the fully discharged (lower) and charged (upper) states, recorded during the tenth cycle [discharge and charge: 10C at 55°C].

To clarify the effects of the C-rate on the discharge-charge processes, we studied the electrochemical performances of discharging and charging at 0.1C and 10C, respectively, and discharging and charging at 10C and 0.1C, respectively. The obtained discharge-charge curves of BiF_3/C at 55°C during the ten cycles are presented in Fig. 5. In the former process (Fig. 5(a)), the charge capacity drastically decreased between the first (253 mAh g^{-1}) and the tenth (58 mAh g^{-1}) cycles. The charge capacities recorded during the ten cycles were similar to those found at 10C (Fig. 3(c)). Therefore, charging at 10C drastically decreased the capacity during cycling, regardless of the C-rate during discharge. The electrochemical performance of the latter process (discharging at 10C and charging at 0.1C) clarifies the effects of the C-rate on the cycling performance (Fig. 5(b)). Even during the tenth cycle, this process yielded a much higher discharge capacity (210 mAh g^{-1}) than discharging and charging at 10C (31 mAh g^{-1}; see Fig. 3(c)). Thus, as long as the charge reaction progressed, the discharge reaction progressed even at 10C. Clearly, the C-rate performance was much higher in the discharge process than in the charge process.
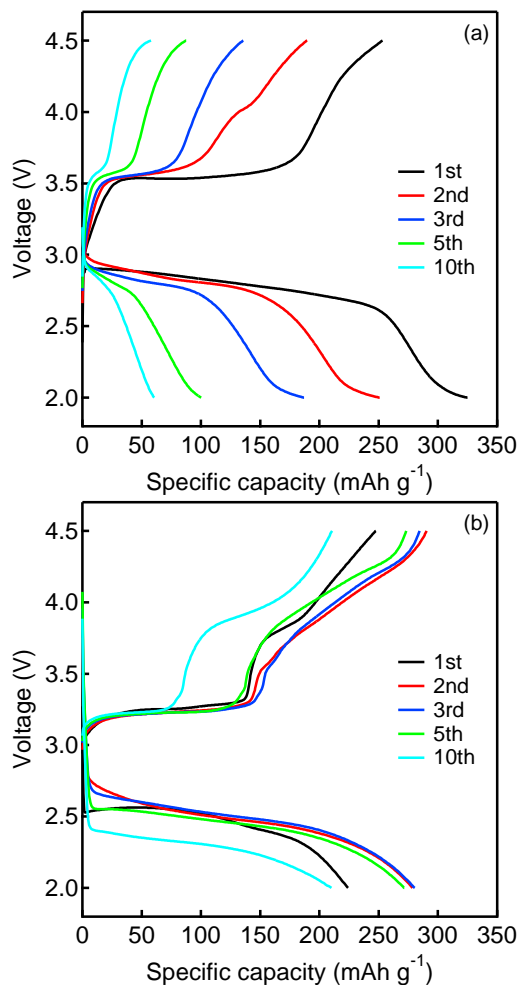
Fig. 5. Discharge-charge curves of BiF$_3$/C at 55°C and various C-rates over ten cycles:

(a) discharge: 0.1C, charge: 10C; and (b) discharge: 10C, charge: 0.1C. Black, red, blue,

green, and aqua curves are the discharge-charge curves obtained in the first, second,

third, fifth, and tenth cycles, respectively.

3.4. Crystal structure of the BiF$_3$/C electrode at a high C-rate

To confirm the behavioral difference of the discharge and charge reactions at

15

high C-rates, we analyzed the crystal structures of the active materials by XRD. Fig. 6 shows the XRD patterns during the tenth cycle of the BiF_3/C electrode during the discharging and charging cycles at 0.1 and 10C, respectively (Fig. 6(a)), and during discharging and charging cycles at 10 and 0.1C, respectively (Fig. 6(b)). All of the peaks in the fully discharged state of Fig. 6(a), (except for the BiF_3 peak at $2\theta = 28°$) were assigned to Bi metal, indicating good progression of the discharge reaction. In contrast, the diffraction pattern in the fully charged state did not significantly differ from that of the fully discharged state (c.f. upper and lower patterns in Fig. 6(a)). This indicates negligible progression of the charge reaction at the higher C-rate. However, discharging at 10C and charging at 0.1C altered the reaction behavior (Fig. 6(b)). In the fully discharged state, the pattern was indistinguishable from that of Fig. 6(a). However, changing the C-rate from 10 to 0.1C enabled the charge reaction in the tenth cycle, as evidenced by the peaks in the charged state (upper pattern in Fig. 6(b)). All of these peaks were attributed to BiF_3. Therefore, whereas the discharge reaction progressed even at a high C-rate (10C), the charge reaction hardly progressed at 10C, as also observed in the discharge-charge measurements (Figs. 5(a) and (b)).
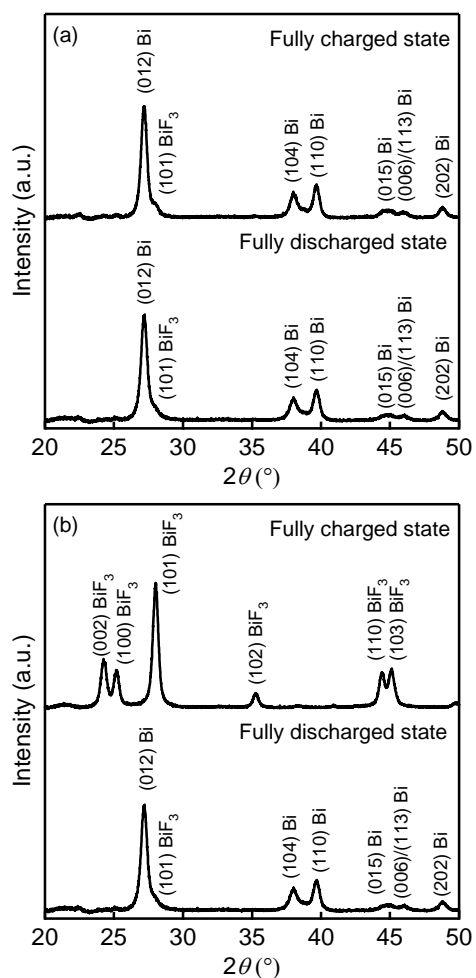
Fig. 6. XRD patterns of BiF₃/C in the fully discharged (lower) and charged (upper) states, recorded during the tenth cycle at 55°C: (a) discharge: 0.1C, charge: 10C; and (b) discharge: 10C, charge: 0.1C.

3.5. Possibility of crack formation in the active material during the discharge-charge reaction

The results of the electrochemical and XRD measurements, which are shown in

17

Figs. 5 and 6, indicate that the discharge reaction progressed even at a high C-rate (10C), whereas the charge reaction hardly proceeded at 10C. It has been proposed that the volume of BiF_3 greatly changes during the discharge-charge processes [29]. The large volume change of active material is accompanied by crack formation and subsequent isolation of the active material [38, 39], separating it from the AB after cycling [39, 40]. It is possible that the crack formation is responsible for the decrease in the cycling capacity of our electrodes. The cracking was directly observed using the SEM for other active material [38, 39]. Therefore, we tried to observe the change in particle configuration of the active material after the discharge-charge reactions. However, due to small particle size of the active material and nanocomposite formation between the active material and AB in our electrode, the change in particle configuration of the active material could not be observed. Therefore, we studied the possibility of crack formation by calculating the interaction between Bi and BiF_3.

Fig. 7 shows the DFT-optimized structure of a system containing Bi and BiF_3 layers. Fig. 8 shows the change in the total energy upon changing the z position of Bi layers. The zero displacement value was determined from the position of the Bi layer in the optimized structure shown in Fig. 7. The closest distance between a Bi atom in the Bi layer and a F atom at the surface of the BiF_3 layer in the optimized structure (Fig. 7)

is 0.32 nm. This distance is much greater than the length of the Bi−F bonds in the BiF_3

hexagonal crystal (0.24 nm). By approaching the Bi layer to the BiF_3 layer from the

optimized structure (displacement = zero), the total energy distinctly increased, as

shown in Fig. 8. A decrease in the distance between the Bi and BiF_3 layers causes

instability. Moreover, the retraction of the Bi layers from BiF_3 in the optimized structure

causes the increase in the total energy (Fig. 8). These results show that the contact

between the Bi and BiF_3 layers is not energetically stable. During the discharge-charge

reactions of the BiF_3 electrode, an interface between Bi and BiF_3 is formed. Our

calculation results show that as the interface is unstable, separation of the Bi and BiF_3

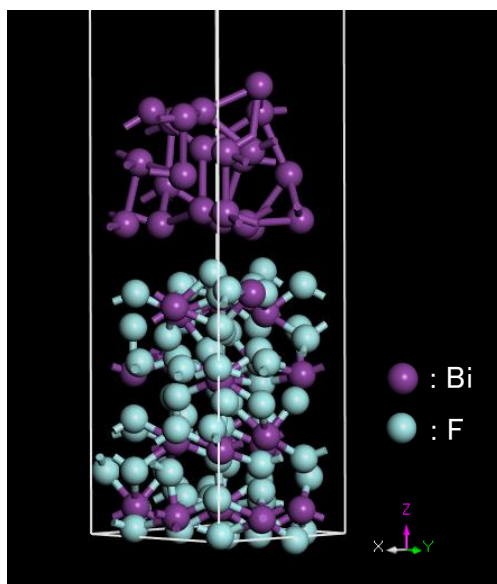phases and crack formation should occur during the discharge-charge reactions.

Fig. 7. The optimized structure of a system with Bi and BiF_3 layers. The Bi and BiF_3 layers are composed of Bi_{22} and $Bi_{24}F_{72}$ atoms, respectively. Purple and aqua balls denote Bi and F atoms, respectively.
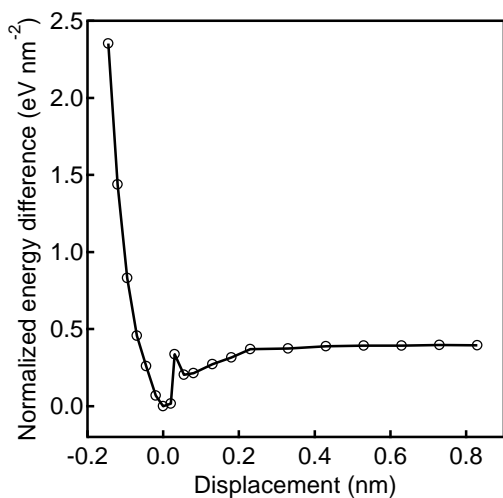
Fig. 8. Difference in total energy with the displacement of the Bi layer toward the z direction. The energy is normalized by area. The negative and positive displacement values refer to the Bi layer approaching and retracting from the BiF_3 layers, respectively. The zero displacement value and energy change are determined at the position and energy of the optimized structure shown in Fig. 7.

3.6. Difference of high C-rate performance between discharge and charge processes

The discharge and charge reactions of BiF_3 are given below [23–25]:

Discharge reaction: $BiF_3 + 3Li^+ + 3e^- \rightarrow Bi + 3LiF$ (ii)

Charge reaction: $Bi + 3LiF \rightarrow BiF_3 + 3Li^+ + 3e^-$ (iii)
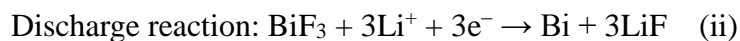
As shown in Fig. 1, the formation of nanocomposite with AB was effective in improving the electrochemical properties, especially the charge process. This indicates that the electronic conductive path is essential for the electrochemical reaction. The

20

electrochemical reaction started at the interface between the active material and electrolyte, and proceeded from the surface to bulk of active material [25]. During the charge process, insulating BiF_3 is formed on the surface of Bi metal and LiF particles. Once the surface of the Bi particle is covered with insulating BiF_3, the charge reaction hardly progressed due to the high IR drop. In contrast, during the discharge process, metallic Bi was formed on the surface of BiF_3. The metallic Bi was used as an electronic conduction path; therefore, high capacity was maintained at high C-rate after cycling.

Also, a crack formation in the active materials would have influence to the cyclic performance. During the discharge and charge process, the interface of Bi and BiF_3 would be formed. As described in section 3.5, this interface is not stable. The active material should contain cracks to separate Bi and BiF_3 phases. The formation of crack would decrease the electronic conductivity of the electrode due to the separation from AB. This would have influence to the cyclic performance of BiF_3 electrode.

4. Conclusions

This work has examined the difference of high C-rate performance of BiF_3/C, a nanocomposite of BiF_3 and AB, between discharge and charge processes. During the

first cycle, the discharge and charge reactions of BiF_3/C progressed even at 10C, but at high C-rates, the performance of the charge reaction deteriorated during cycling. Indeed, the charge capacity was drastically decreased during cycling at 10C, regardless of the C-rate during discharging. In contrast, at a charging C-rate of 0.1, the BiF_3/C exhibited high discharge capacity even at 10C. The discharge–charge reactions of BiF_3 were accompanied by a large volume change, and as a result, the contact between BiF_3 and AB was lost during cycling. However, a new electronic conductive path was formed by the Bi metal other than AB; therefore, a high discharge capacity was obtained even at high C-rates after cycling.

Acknowledgements

23

experiments.

References

[1] Y. Nishi, J. Power Sources 100 (2001) 101−106.

[2] J. Wang, J. Yang, C. Wan, K. Du, J. Xie, N. Xu, Adv. Funct. Mater. 13 (2003) 487−492.

[3] B. Diouf, R. Pode, Renewable Energy 76 (2015) 375−380.

[4] H. Li, P. Balaya, J. Maier, J. Electrochem. Soc. 151 (2004) A1878−A1885.

[5] F. Badway, A. N. Mansour, N. Pereira, J. F. Al-Sharab, F. Cosandey, I. Plitz, G. G. Amatucci, Chem. Mater. 19 (2007) 4129−4141.

[6] N. Yabuuchi, M. Sugano, Y. Yamakawa, I. Nakai, K. Sakamoto, H. Muramatsu, S. Komaba, J. Mater. Chem. 21 (2011) 10035−10041.

[7] L. Liu, X. Wang, X. Wang, X. Wang, F. Tian, L. Yi, Electrochim. Acta 56 (2011) 7437−7441.

[8] D. H. Lee, K. Carroll, S. Calvin, S. Jin, Y. S. Meng, Electrochim. Acta 59 (2012) 213−221.

[9] M. Sina, K. W. Nam, D. Su, N. Pereira, X. Q. Yang, G. G. Amatucci, F. Cosandey, J. Mater. Chem. A 1 (2013) 11629−11640.

[10] R. Ma, M. Wang, P. Tao, Y. Wang, C. Cao, G. Shan, S. Yang, L. Xi, J.C.Y. Chung, Z. Lu, J. Mater. Chem. A 1 (2013) 15060−15067.

[11] B. Hu, X. Wang, Q. Wei, H. Shu, X. Yang, Y. Bai, H. Wu, Y. Song, L. Liu, J. Alloys Compd. 579 (2013) 18–26.

[12] M.Y. Cheng, Y.S. Ye, T.M. Chiu, C.J. Pan, B.J. Hwang, J. Power Sources 253 (2014) 27–34.

[13] Y. Zhao, T. Liu, H. Xia, L. Zhang, J. Jiang, M. Shen, J. Ni, L. Gao, J. Mater. Chem. A 2 (2014) 13854–13858.

[14] J. Ni, Y. Zhao, T. Liu, H. Zheng, L. Gao, C. Yan, L. Li, Adv. Energy Mater. 4 (2014) 1400798.

[15] W. Zuo, W. Zhu, D. Zhao, Y. Sun, Y. Li, J. Liu, X. W. D. Lou, Energy Environ. Sci. 9 (2016) 2881–2891.

[16] X. Fan, Y. Zhu, C. Luo, T. Gao, L. Suo, S.C. Liou, K. Xu, and C. Wang, J. Power Sources 307 (2016) 435–442.

[17] A. Pohl, M. Faraz, A. Schroder, M. Baunach, W. Schabel, A. Guda, V. Shapovalov, A. Soldatov, V.S.K. Chakravadhanula, C. Kubel, R. Witte, H. Hahn, T. Diemant, R.J. Behm, H. Emerich, M. Fichtner, J. Power Sources 313 (2016) 213–222.

[18] W. Fang, N. Zhang, L. Fan, K. Sun, J. Power Sources 333 (2016) 30–36.

[19] S. Bohme, K. Edstrom, L. Nyholm, J. Electroanal. Chem. 797 (2017) 47–60.

[20] J. Ding, S.A. Abbas, C. Hanmandlu, L. Lin, C.S. Lai, P.C. Wang, L.J. Li, C.W. Chu,

C.C. Chang, J. Power Sources 348 (2017) 270–280.

[21] H. Liang, J. Ni, L. Li, Nano Energy 33 (2017) 213–220.

[22] J. Ni, X. Bi, Y. Jiang, L. Li, J. Lu, Nano Energy 34 (2017) 356–366.

[23] M. Bervas, F. Badway, L. C. Klein, G. G. Amatucci, Electrochem. Solid-State Lett. 8 (2005) A179–A183.

[24] M. Bervas, L. C. Klein, and G. G. Amatucci, J. Electrochem. Soc. 153 (2006) A159–A170.

[25] M. Bervas, A. N. Mansour, W. S. Yoon, J. F. Al-Sharab, F. Badway, F. Cosandey, L. C. Klein, G. G. Amatucci, J. Electrochem. Soc. 153 (2006) A799–A808.

[26] A.J. Gmitter, F. Badway, S. Rangan, R.A. Bartynski, A. Halajko, N. Pereira, G.G. Amatucci, J. Mater. Chem. 20 (2010) 4149–4161.

[27] H. Konishi, T. Minato, T. Abe, Z. Ogumi, ChemistrySelect 2 (2017) 3504–3510.

[28] B. Hu, X. Wang, Y. Wang, Q. Wei, Y. Song, H. Shu, X. Yang, J. Power Sources 218 (2012) 204–211.

[29] A.J. Gmitter, J. Gural, G.G. Amatucci, J. Power Sources 217 (2012) 21–28.

[30] B. Hu, X. Wang, H. Shu, X. Yang, L. Liu, Y. Song, Q. Wei, H. Hu, H. Wu, L. Jiang, X. Liu, Electrochim. Acta 102 (2013) 8–18.

[31] J. K. Ko, A. Halajko, M. F. Parkinson, G. G. Amatucci, J. Electrochem. Soc. 162

(2015) A149−A154.

[32] H. Konishi, T. Minato, T. Abe, Z. Ogumi, ChemistrySelect 2 (2017) 6399−6406.

[33] Z. Yang, S. Tan, Z. Zhang, Y. Huang, X. Wang, Mater. Chem. Phys. 173 (2016) 291−297,

[34] H. Du, X. Sun, X. Liu, X. Wu, J. Wang, M. Tian, A. Zhao, Y. Luo, J. Yang, B. Wang, J.G. Hou, Nat. Commun. 7 (2016) 10814.

[35] S.J. Clark, M.D. Segall, C.J. Pickard, P.J. Hasnip, M.J. Probert, K. Refson, M.C. Payne, Z. Kristallogr. 220 (2005) 567−570.

[36] B.G. Pfrommer, M. Cote, S.G. Louie, M.L. Cohen, J. Comput. Phys. 131 (1997) 233−240.

[37] J.P. Perdew, K. Burke, M. Ernzerhof, Phys. Rev. Lett. 77 (1996) 3865−3868.

[38] H. Li, X. Huang, L. Chen, Z. Wu, Y. Liang, Electrochem. Solid-State Lett. 2 (1999) 547−549.

[39] W. R. Liu, Z. Z. Guo, W. S. Young, D. T. Shieh, H. C. Wu, M. H. Yang, N. L. Wu, J. Power Sources 140 (2005) 139−144.

[40] J. H. Ryu, J. W. Kim, Y. E. Sung, S. M. Oh, Electrochem. Solid-State Lett. 7 (2004) A306−A309.

Figure captions

Fig. 1. Initial discharge-charge curves of BiF_3 and BiF_3/C at 0.1C and at 25 and 55°C [BiF_3 at 25°C (black curve), BiF_3/C at 25°C (red curve), and BiF_3/C at 55°C (blue curve)].

Fig. 2. XRD patterns of BiF_3/C during the initial discharge-charge processes [0.1C at 55°C].

Fig. 3. Discharge-charge curves of BiF_3/C at 55°C and various C-rates over ten cycles: (a) 0.1C, (b) 1C, and (c) 10C. Black, red, blue, green, and aqua curves represent the discharge-charge curves during the first, second, third, fifth, and tenth cycles, respectively.

Fig. 4. XRD patterns of BiF_3/C in the fully discharged (lower) and charged (upper) states, recorded during the tenth cycle [discharge and charge: 10C at 55°C].

Fig. 5. Discharge-charge curves of BiF_3/C at 55°C and various C-rates over ten cycles: (a) discharge: 0.1C, charge: 10C; and (b) discharge: 10C, charge: 0.1C. Black, red, blue,

green, and aqua curves are the discharge-charge curves obtained in the first, second, third, fifth, and tenth cycles, respectively.

Fig. 6. XRD patterns of BiF_3/C in the fully discharged (lower) and charged (upper) states, recorded during the tenth cycle at 55°C: (a) discharge: 0.1C, charge: 10C; and (b) discharge: 10C, charge: 0.1C.

Fig. 7. The optimized structure of a system with Bi and BiF_3 layers. The Bi and BiF_3 layers are composed of Bi_{22} and $Bi_{24}F_{72}$ atoms, respectively. Purple and aqua balls donate Bi and F atoms, respectively.

Fig. 8. Difference in total energy with the displacement of the Bi layer toward the z direction. The energy is normalized by area. The negative and positive displacement values refer to the Bi layer approaching and retracting from the BiF_3 layers, respectively. The zero displacement value and energy change are determined at the position and energy of the optimized structure shown in Fig. 7.